Performance degradation of $Li_x FePO_4$ (x = 0, 1) induced by postannealing

Xiaofei SUN, Youlong XU[∗]**, Xiaoyu ZHENG, Xiangfei MENG, Rui ZHANG**
Electronic Materials Research Laboratory, Key Laboratory of the Ministry of Education & International Center
for Dielectric Research, Xi'an Jiaotong University, Xi'an, P. R. China

Abstract: Olivine $LiFePO_4$ has been studied for more than a decade as a promising cathode material for rechargeable lithium batteries. However, the low electric conductivity and tap density still hinder its large-scale commercialization. Micro-sized $LiFePO_4$ is prepared by an optimized hydrothermal method in this paper. The influence of postannealing on the physicochemical properties of $LiFePO_4$ and $FePO_4$ is investigated to understand the plausible mechanism for performance degradation. It is found that postannealing even chemical delithiation greatly affects the particle size, morphology, pore distribution, surface area, and probably the lattice strain of $Li_x FePO_4$ (x = 0, 1). Consequently, the electrochemical performances of annealed materials are severely deteriorated because of the sluggish lithium diffusion, difficult electrolyte accessibility, and incomplete phase transition during charge/discharge. In addition, the "self-healing" process along with cycling is analyzed by in-situ synchrotron X-ray diffraction.

Key words: Lithium iron phosphate, hydrothermal synthesis, postannealing, chemical delithiation, lithium ion battery, energy storage and conversion

1. Introduction

The rechargeable lithium battery is considered one of the most prospective energy storage technologies because of its high energy density as well as power density.[1] It has been widely used in portable electronics, and is being studied for broad applications in electric vehicles including hybrid electric vehicles and plug-in hybrid electric vehicles.[2] Moreover, it is a potential battery choice for high efficiency stationary energy storage. On one hand, it could balance the power grid by charging at valley load while discharging at peak load. On the other hand, it can be used to store and utilize the intermittent renewable energy such as solar, wind, and tide.[3] Moreover, credible market demand for rechargeable lithium batteries also comes from the sectors of communication, medicine, aerospace, military, power tools, and so on.

As one of the key components, the cathode plays a crucial role in the performance and cost of the overall battery, and is therefore the bottleneck presently constraining the fast development of rechargeable lithium batteries.[4] Layered $LiCoO_2$ has been the most successful cathode material since the commercialization of the lithium ion battery by the Sony Corporation in 1991, but is limited in high energy and high power applications by its low safety, high toxicity, and high cost shortages.[5] Transition metals, e.g., Ni, Mn, and Al, are then introduced into the layered structure, and series of binary and ternary cathodes that have high capacity, high stability, and high safety are obtained by tuning the composition of $LiA_x B_y C_z O_2$ (A, B, C = Ni, Co, Mn, Al, etc.; x + y + z = 1).[6] Meanwhile, spinel $LiMn_2 O_4$ and its high voltage derivative $LiNi_{0.5} Mn_{1.5} O_4$ are well-

∗Correspondence: ylxu@mail.xjtu.edu.cn

known cathode materials for their low cost merits. [7] Polyanion compounds constructed by MO_6 (M is a transition metal) octahedra and XO_4 (X = P, Si, S, As, Mo, W, etc.) tetrahedra in open 3-dimensional frameworks are another group of prospective cathode materials because of their superior thermal stability. [8] Moreover, the redox potential could be flexibly tailored by proper design of M and X. Besides silicates (Li_2MSiO_4, M = Fe, Mn, Co, etc.), [9] borates ($LiMBO_3$, M = Fe, Co, Mn, etc.), [10] fluorophosphates ($LiVPO_4F$), and fluorosulfates ($LiMSO_4F$, M = Fe, Co, Mn, Ni, etc.), [11,12] phosphates ($LiMPO_4$, M = Fe, Mn, Co, Ni, etc.) are the first and most studied polyanion-type cathode materials. [13]

Amongst these, olivine $LiFePO_4$ is advantageous due to its high specific capacity (theoretically 170 mA h g^{-1}), flat charge/discharge plateau ($\sim$3.45 V vs. Li/Li^+, hereafter), high thermal and chemical stabilities, and environmentally friendliness. [14] Since the pioneering work by Goodenough's group in 1997, [15] $LiFePO_4$ has been intensively investigated for high efficiency energy storage applications. [16] However, the low electric conductivity hinders its large-scale commercialization. Lithium ions (Li^+) were predicted diffuse in one-dimensional tunnels along the [010] direction by first principle computation, [17,18] which has been experimentally verified by Yamada's group. [19] Meanwhile, shrink-core, platelet type, domino cascade models were introduced successively to interpret the 2-phase reaction process during charge/discharge. [20−23] Importantly, the solid solution phase was found at the beginning of charge/discharge. [24] Gu et al. also observed the lithium staging phenomenon in partially delithiated $LiFePO_4$ analogously in layered intercalation compounds. [25] Recently, ab-initio calculation revealed the suppression of phase separation due to the nonequilibrium Li incorporation during discharging. [26,27] Therefore, the 1-D lithium diffusion channel could be easily blocked by adjacent atoms such as Fe^{2+}, and consequently deteriorates the electrochemical performance of $LiFePO_4$. In addition to surface coating and bulk doping, [28−30] particle down-sizing has been successfully employed to shorten the lithium diffusion path so as to expedite lithium migration during charge/discharge. [31,32] While the tap density of $LiFePO_4$ is dramatically decreased in nanoscale, so is the volumetric energy/power density. [33,34]

It is therefore of great interest and importance to investigate the physicochemical properties of large particle $LiFePO_4$, so as to look into the mechanisms of performance degradation comparing with their nano-sized counterparts, and accordingly to design high density high performance $LiFePO_4$ cathodes. In this paper, micro-sized $LiFePO_4$ is prepared by an optimized hydrothermal method. The influence of postannealing as well as chemical delithiation on the structure, particle size, morphology, pore distribution, surface area, and electrochemical performance of intrinsic Li_xFePO_4 (x = 0, 1) is comparatively studied.

2. Results and discussion

Pristine $LiFePO_4$ (LFP) was synthesized by an optimized hydrothermal route. The annealed $LiFePO_4$ (A-LFP) was prepared by postannealing of LFP at 700 °C followed by liquid nitrogen quenching. $FePO_4$ (FP) was derived by chemical delithiation of A-LFP with NO_2BF_4 in acetonitrile. The annealed $FePO_4$ (A-FP) was obtained via annealing of FP at 300 °C. The high resolution synchrotron XRD pattern in Figure 1 indicates that all the samples are phase-pure olivine phosphates without any detectable impurity. They are well crystallized in agreement with the reference patterns from ICSD. No Fe^{2+} was oxidized during postannealing of $LiFePO_4$ because pristine LFP was sealed in an ampoule under good vacuum protection. The annealing temperature of FP was chosen at 300 °C to avoid phase transition from orthorhombic to trigonal at temperatures higher than 450 °C. [35] Moreover, no obvious crystalline difference was found after postannealing for LFP or FP.
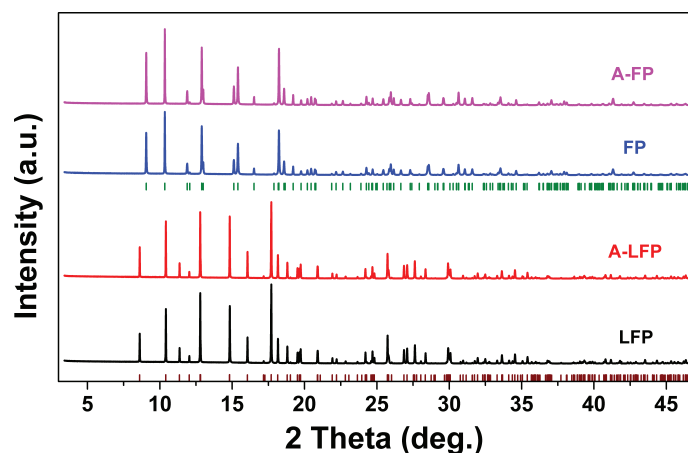
Figure 1. High resolution synchrotron XRD patterns of pristine LFP, A-LFP, FP, and A-FP. The wavelength is 0.7751922 Å. The vertical lines at the bottom of each group indicate the reference patterns of $LiFePO_4$ and $FePO_4$ from ICSD, respectively.

Figures 2a–2d exhibit the FESEM images while the particle size distributions are shown in Figures 3a–3d. The as-prepared LFP possesses a distorted diamond morphology with a typical particle size of $D_{50} = 1.55$ μm.
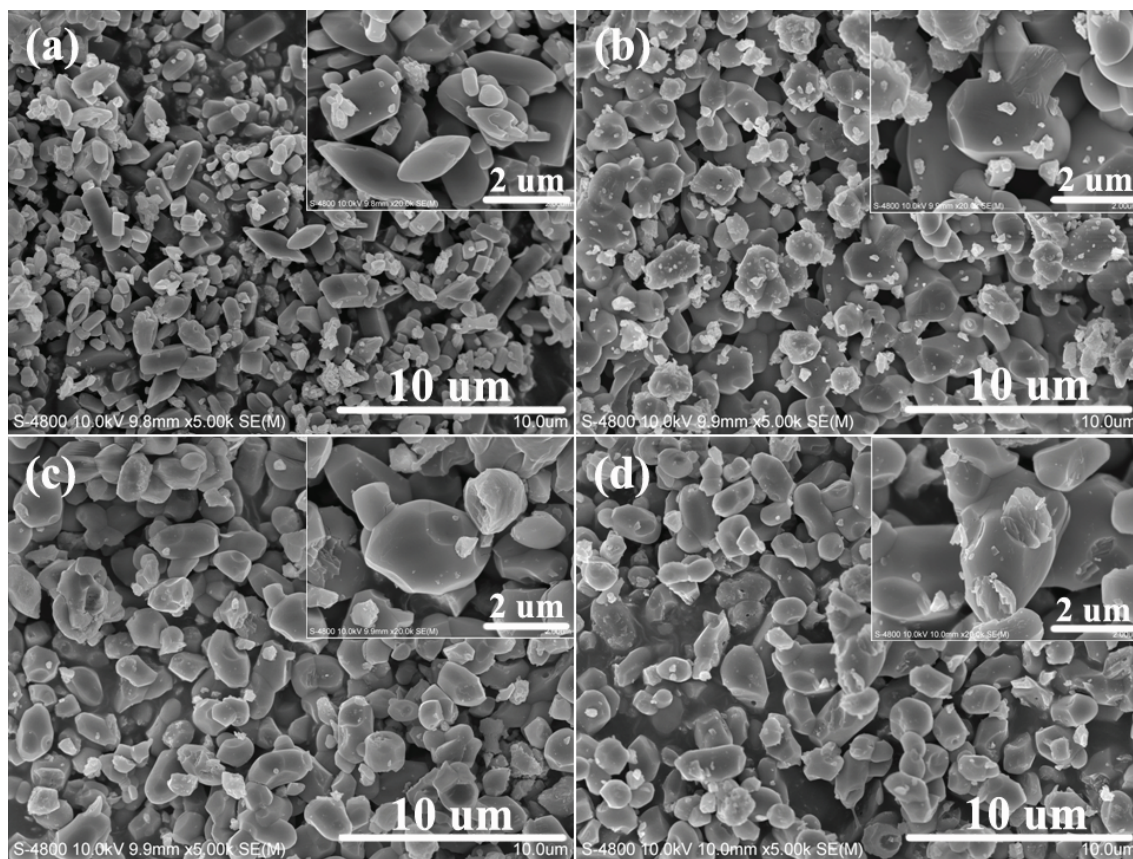
Figure 2. FESEM images of pristine LFP (a), A-LFP (b), FP (c), and A-FP (d). The inset of each image shows the enlarged picture at a higher magnification.

The particle morphology changes to quasi-sphere and the particle size increases to $D_{50} = 2.13$ μm after the high temperature equilibration of LFP at 700 °C for 24 h. Due to the long time annealing, the particles are found agglomerated with a much wider size distribution. Note that liquid nitrogen quenching could also contribute to some of these transformations. Comparing with A-LFP, chemical delithiation by NO_2BF_4 does not cause any obvious change in the particle morphology, but a large number of the agglomerated ultrabig A-LFP particles are dispersed and crushed by the mechanical and chemical forces during delithiation.[36] As a result, the particle size distribution becomes more homogeneous and the number of large particles is remarkably decreased while the nominal mean particle size is slightly increased to $D_{50} = 2.72$ μm. Lastly, low temperature annealing at 300 °C does not noticeably affect the particle size or morphology of FP.
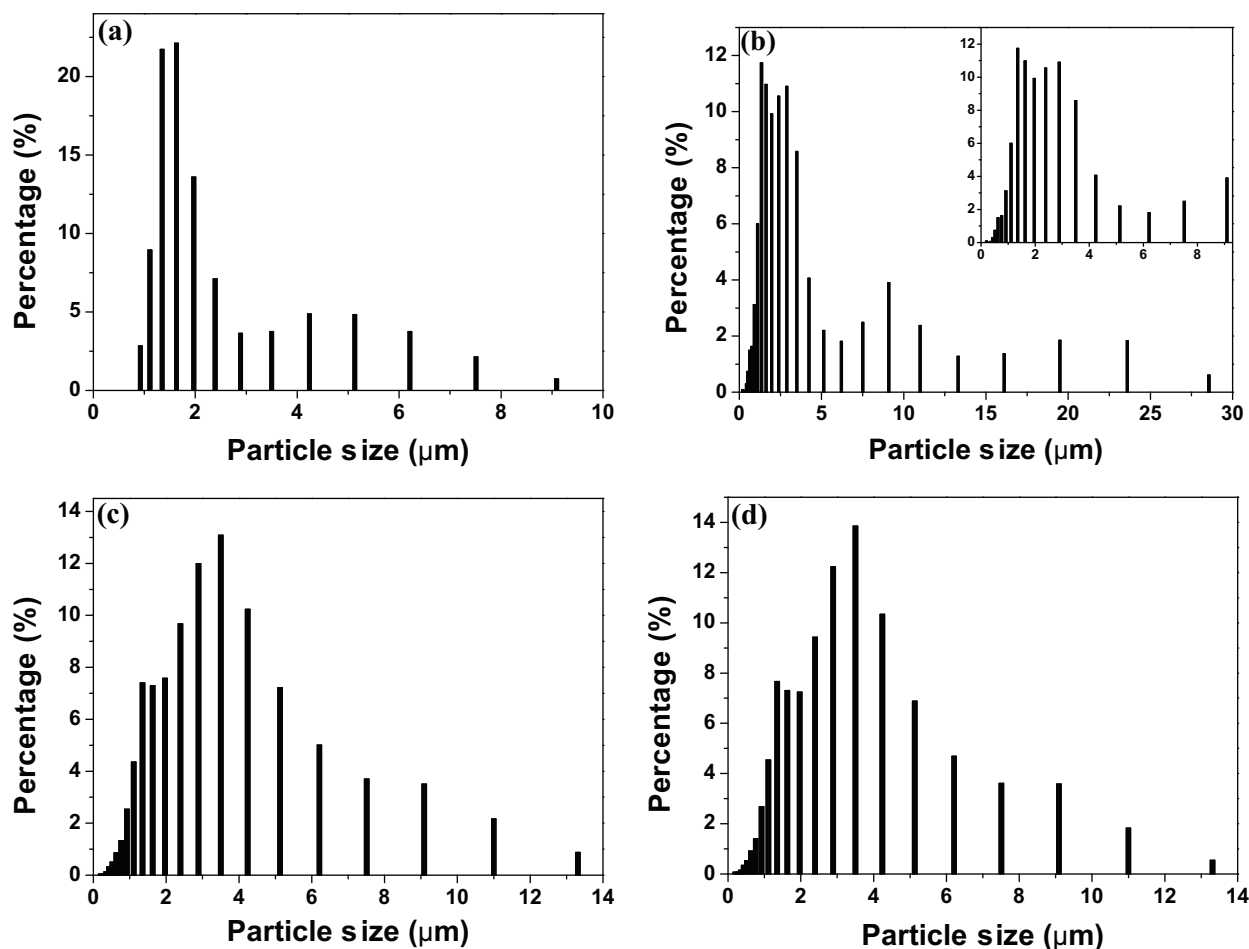
Figure 3. Particle size distribution of pristine LFP (a), A-LFP (b), FP (c), and A-FP (d). The small size region of A-LFP (b) is zoomed in on for clear illustration.

The battery performances of these samples were studied by prototype batteries using lithium metal as the anodes. The charge/discharge curves of the first 5 cycles at 0.1 C (1 C = 170 mA g^{-1}, hereafter) rate are shown in Figures 4a–4d. Pristine LFP shows a typical flat charge/discharge plateau as in the literature with the specific discharge capacity of $\sim$146–148 mA h g^{-1}.[37] The capacity is acceptable for micrometer-sized LiFePO$_4$ without any modification such as surface coating or bulk doping. The A-LFP shows a slope-like charge profile in the first cycle and releases a specific discharge capacity of 110 mA h g^{-1}, which increases to 120 mA h g^{-1}

in the fifth cycle. The specific charge capacity of FP in the first cycle is only 1.5 mA h g^{-1}, indicating that lithium is almost completely removed from A-LFP by NO_2BF_4. The specific discharge capacity increases from 121 mA h g^{-1} to 144 mA h g^{-1} after 5 cycles. Similar to LFP, the electrochemical performance of FP degrades severely after postannealing. The specific discharge capacity of A-FP drops dramatically to 90–97 mA h g^{-1} with slight differences among different cycles. One needs to note that the slope-like charge/discharge profiles are also observed in the first several cycles of FP and A-FP. The rate capabilities along with cycling are plotted in Figure 5. In good agreement, LFP and FP are proved again to have better capacitive performance at each rate compared with their annealed counterparts. After 100 cycles at 1 C, both LFP and FP retrained $\sim$91% of their initial capacities. It is interesting that pristine LFP shows the best overall battery performance among the 4 samples.
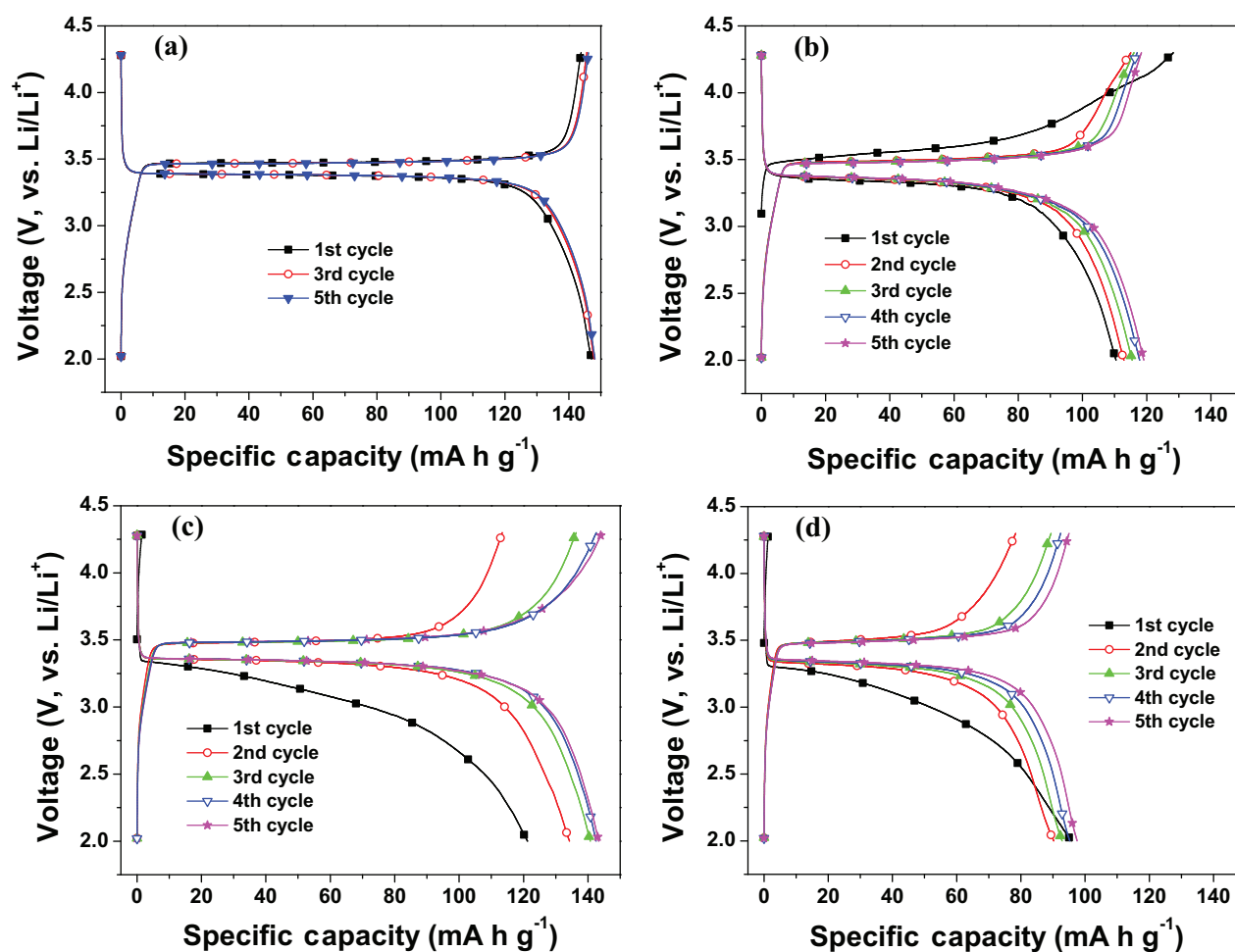

Figure 4. Room temperature charge/discharge curves at 0.1 C rate of pristine (a) LFP, (b) A-LFP, (c) FP, and (d) A-FP.

CR2016 coin cells were made to study the kinetics by EIS in Figure 6. The cathodes for EIS measurements were formed by 70 wt.% active material ($LiFePO_4$ or $FePO_4$), 20 wt.% acetylene black, and 10 wt.% polyvinylidene fluoride (PVDF). The spectra were collected at the open circuit voltage (OCV) after a rest of 6 h. They are typically simulated by the equivalent circuit of $R_s(C_{sei}R_{sei})(QR_{ct})(C_eR_e)Z_w(C_bR_b)$,[11] where Rs represents the resistance of Li^+ and electrons passing through the electrolyte, separator, and externals; C_{sei}
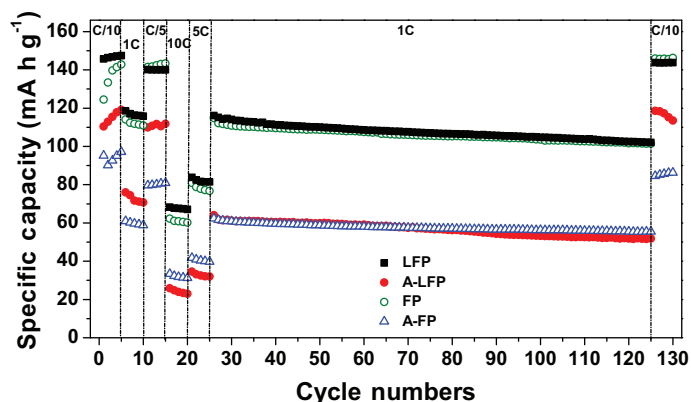
Figure 5. Room temperature rate capability and cycling performance of Li_xFePO_4 (x = 0, 1). The potential window is 2.0–4.3 V (vs. Li/Li^+).

and R_{sei} are the capacitance and resistance of the solid electrolyte interface (SEI) layer, respectively; Q (constant phase element (CPE)) and R_{ct} are the charge transfer capacitance and resistance, respectively; C_e and R_e are the capacitance and resistance related to electron transportation in the active material, respectively; Z_w is the Warburg impedance associated with Li^+ diffusion; and C_b and R_b are the capacitance and resistance, respectively, concerning structure change of the active material. One needs to note an insertion capacitance C_{int} corresponding to the irreversible accumulation and consumption of Li^+ is required to fit the initial EIS of A-LFP. The simulated results are compared in the Table.
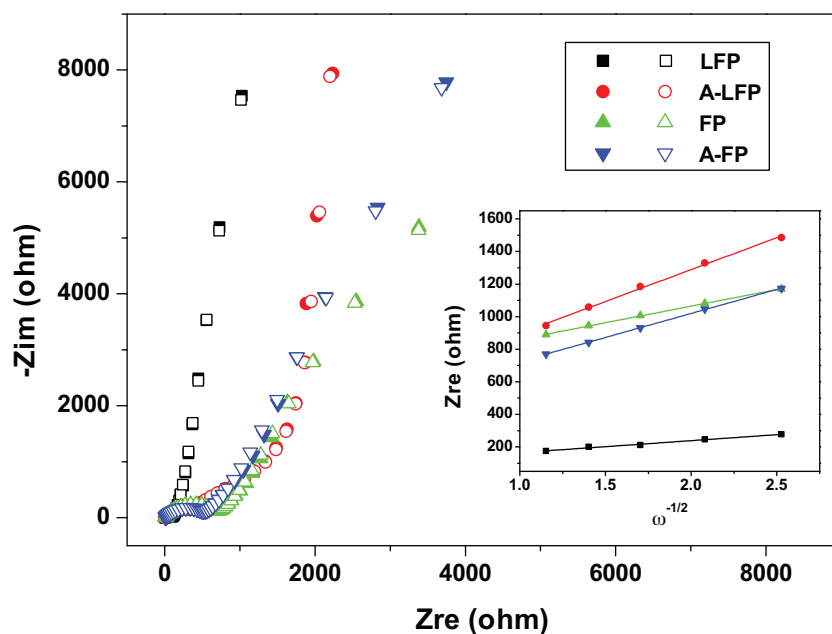
Figure 6. Electrochemical impedance spectrograms of pristine LFP, A-LFP, FP, and A-FP. Solid and hollow scatters represent the measured and simulated data, respectively. The inset shows the Zre $\sim \omega^{-1/2}$ relationship in the low frequency region.

Table. EIS simulation results from Figure 6.

	LFP	A-LFP	FP	A-FP
R_s (Ω cm^2)	6.72	7.695	6.982	10.97
C_{sei} (F cm^{-2})	1.322×10^{-6}	6.032×10^{-7}	2.822×10^{-3}	1.956×10^{-3}
R_{sei} (Ω cm^2)	3.054	5.893	1.234×10^4	2.722×10^4
CPE, Yo (S s^n cm^{-2})	7.53×10^{-6}	3.645×10^{-4}	6.807×10^{-6}	7.71×10^{-6}
n	0.9307	0.5904	0.7936	0.8197
R_{ct} (Ω cm^2)	26.1	1742	612	415.6
C_e (F cm^{-2})	1.57×10^{-3}	6.533×10^{-4}	2.012×10^{-6}	1.978×10^{-6}
R_e (Ω cm^2)	1.415×10^5	2.019×10^4	35.88	44.45
Z_w (S s$^{0.5}$ cm^{-2})	3.952×10^{-3}	6.16×10^{-3}	1.48×10^{-3}	1.094×10^{-3}
C_b (F cm^{-2})	1.042×10^{-5}	4.203×10^{-6}	4.278×10^{-7}	1.21×10^{-6}
R_b (Ω cm^2)	56.57	33.26	12.35	9.458
C_{int} (F cm^{-2})		1.469×10^{-3}		
χ^2	1.431×10^{-3}	1.527×10^{-3}	1.268×10^{-3}	1.616×10^{-3}

The lithium diffusion coefficient (D) could be calculated by the following equation:

$$D = \frac{R^2 T^2}{2A^2 n^4 F^4 C^2 \sigma^2},\tag{1}$$

where R is the gas constant, T is the temperature (K), A is the surface area of the cathode, n is the number of electrons per molecule involved in the redox reaction, F is Faraday constant, C is the Li$^+$ concentration (2.27×10^{-3} mol cm^{-3}, 1.94×10^{-3} mol cm^{-3}, 1.76×10^{-3} mol cm^{-3}, and 1.85×10^{-3} mol cm^{-3}, respectively, for LFP, A-LFP, FP, and A-FP), and σ is the Warburg factor that is associated with Z':

$$Z' = R_D + R_L + \sigma \omega^{-1/2},\tag{2}$$

where ω is the frequency. The relationship of Z' with the reciprocal square root of the frequency ($\omega^{-1/2}$) in the low frequency region is plotted in the inset of Figure 6. Linear fitting indicates the slope corresponding to σ is 91.22, 391.60, 203.39, and 302.94 for LFP, A-LFP, FP, and A-FP, respectively. The Li$^+$ diffusion coefficients are thus calculated to be 4.68×10^{-13} cm^2 s^{-1}, 3.48×10^{-14} cm^2 s^{-1}, 1.57×10^{-13} cm^2 s^{-1}, and 6.39×10^{-14} cm^2 s^{-1}, respectively.

Therefore, pristine LFP has the fastest Li$^+$ diffusion rate because of the favorable particle shape and the uniform particle distribution. It seems from the Table that electron transportation (R_e) contributes a large proportion of the resistance. This is understandable since these intrinsic materials were prepared without any surface coating or bulk doping modifications. In return, it verifies the feasibility of increasing electronic conductivity in promoting the battery performance of LiFePO$_4$.[28] A-LFP has the lowest Li$^+$ diffusion coefficient and the highest charge transfer resistance (R_{ct}) with an additional C_{int} due to the agglomerated large particles and the sphere-like morphology that is unfavorable for Li$^+$ migration. Consequently, it shows poor electrochemical performance. After chemical delithiation, a significant growth in R_{sei} is observed for both FP and A-FP, while the latter shows a slower Li$^+$ diffusion rate and thus worse battery performance.

To fully understand the performance variation along with these treatments, the specific surface area and pore size distribution are measured using N$_2$ sorption isotherms and calculated using the BET method. The N$_2$ adsorption–desorption isotherms and pore size distributions are shown in Figures 7a–7d. The BET surface

area of pristine LFP is 1.95 m^2 g^{-1}, while that of A-LFP is noticeably decreased to 1.18 m^2 g^{-1} possibly due to the morphology rearrangement and particle agglomeration after high temperature annealing. Moreover, the pore size of A-LFP gets smaller with a narrower distribution compared with pristine LFP. The chemically derived FePO$_4$ from A-LFP has the largest specific surface area of 4.14 m^2 g^{-1} with mainly mesopores less than 50 nm. The mechanical and chemical interactions during chemical delithiation play important roles in dispersing and homogenizing the agglomerated ultralarge A-LFP particles.[36] The mesopores are expediential for electrolyte penetration. Hence, the electrochemical performance is greatly improved for FP. Finally, the BET surface area of FePO$_4$ is reduced to 2.04 m^2 g^{-1} by postannealing at 300 °C, and a lot of macropores are presented with a much wider pore size distribution from 20 nm to 200 nm. Although the main particles are as large as tens of micrometers, there are also smaller particles in LFP and FP as shown in Figures 2 and 3. Mesopores are then formed among these smaller particles. However, the smaller particles crystallize and merge into larger particles along with annealing, and the mesopores are consequently decreased in the annealed materials. Note also that all these samples are of low specific surface areas in general.
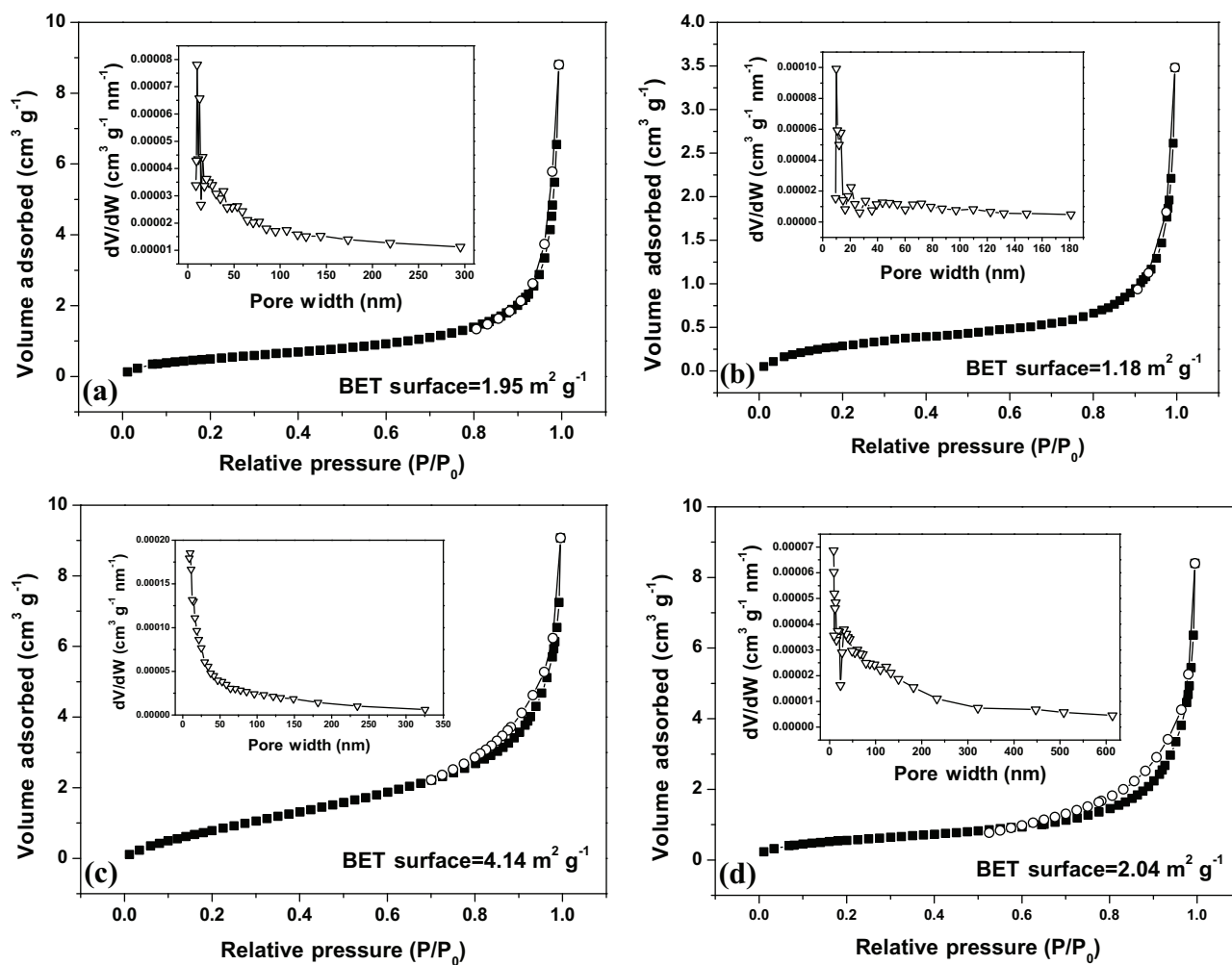

Figure 7. N$_2$ adsorption–desorption isotherms and pore size distributions (insets) of pristine LFP (a), A-LFP (b), FP (c), and A-FP (d). The BET surface area of each sample is also specified.

One still needs to pay attention to the "self-healing" process during electrochemical cycling. It starts from A-LFP and becomes more severe in delithiated materials including both FP and A-FP. As already shown in Figures 4 and 5, the specific discharge capacity increases in the first several cycles and stabilizes at a certain level thereafter for A-LFP, FP, and A-FP. Moreover, the charge/discharge curves change from slope-like profiles to flat plateaus along with this process. In Figure 8a, in-situ synchrotron XRD was used to track the detailed structure change during charge/discharge of A-FP in the first 3 cycles. Galvanostatic cycling was operated at $\sim$0.2 C rate between 2.0 V and 4.4 V as shown in Figure 8b. Only a quarter of the collected XRD patterns are depicted except for the mono one in the first charge because nearly all the lithium is removed after chemical delithiation. The slight shift of the (111) peak at $\sim$11.57° during charge/discharge indicates a little solid solution behavior as already discussed.[31] The electrochemical reaction generally follows a 2-phase mechanism. Ideally, the peak intensity of $LiFePO_4$ increases while that of $FePO_4$ decreases until it totally disappears at the end of discharge. The peaks change oppositely during charging. However, the actual patterns deviate from such ideal revolution. During discharge in the first cycle, the (121) and (200) peaks of $FePO_4$ at $\sim$13.58° and $\sim$13.81° are broadened but that of $LiFePO_4$ at $\sim$13.34° does not appear until the battery is nearly half discharged. The delayed appearance of the second phase is far more severe than reported in the literature.[38] Moreover, the 2 high-angle peaks do not vanish but co-exist unexpectedly with the new ones at the end of discharge. The subsequent charge process thus starts from this stage and ends with the removal of roughly the afore-inserted lithium. Therefore, the electrochemical reaction takes place slowly and incompletely. By carefully comparing the XRD patterns at each discharged state, the intensities of (121) and (200) peaks of $LiFePO_4$ at 13.34° gradually increase with the increase in cycle number. This indicates that a little more lithium is possibly inserted along with cycling. Once this "self-healing" process gets equilibrated after several cycles, lithium is (de)inserted in a relatively stable way. That might be the reason for the capacity increase along with cycling in the first several cycles. Interestingly, this phenomenon and thus the related charge/discharge behavior originates from A-LFP and is reserved in the delithiated samples of both FP and A-FP. Unfortunately, the detailed mechanism of how annealing brings about such change is still unclear. One speculation is that the release of lattice strain after postannealing might induce suppression of phase separation during charge/discharge and thus deterioration of the battery performance of Li_xFePO_4 (x = 0, 1).[26,27,39,40]

In summary, although high resolution synchrotron XRD shows no obvious phase structure change, the particle size, morphology, pore distribution, surface area, and electrochemical performance of Li_xFePO_4 (x = 0, 1) vary significantly along with these treatments. It can be seen from the above that, without any modification such as surface coating or atomic doping, pristine LFP exhibits the highest specific capacity, fastest charge/discharge capability, and most stable cyclability, possibly because of the homogeneous distorted diamond-shaped particles and the beneficial pore distribution in addition to the good crystallinity. As identified by Chen et al.,[21] the large diamond surface in hydrothermally synthesized $LiFePO_4$ corresponds to the (010) plane and the so-formed thin [010] platelet greatly facilitates lithium diffusion along the b direction. The particles are uniform in size and morphology. Moreover, the as-prepared $LiFePO_4$ has a certain number of mesopores that are mainly distributed at around 10–70 nm with a specific surface area of about 1.95 m^2 g^{-1}. The mesopores are helpful for electrolyte infiltration and thus Li^+ migration in the electrode. Consequently, pristine LFP shows the highest lithium diffusion coefficient and the best intrinsic battery performance. After high temperature annealing at 700 °C for 24 h followed by liquid nitrogen quenching, the particle morphology is changed to quasi-sphere and the particle size is noticeably increased. Meanwhile, a large number of agglomerates are formed, making the particle size distribution much wider. Hence, the mesopores are substantially reduced and
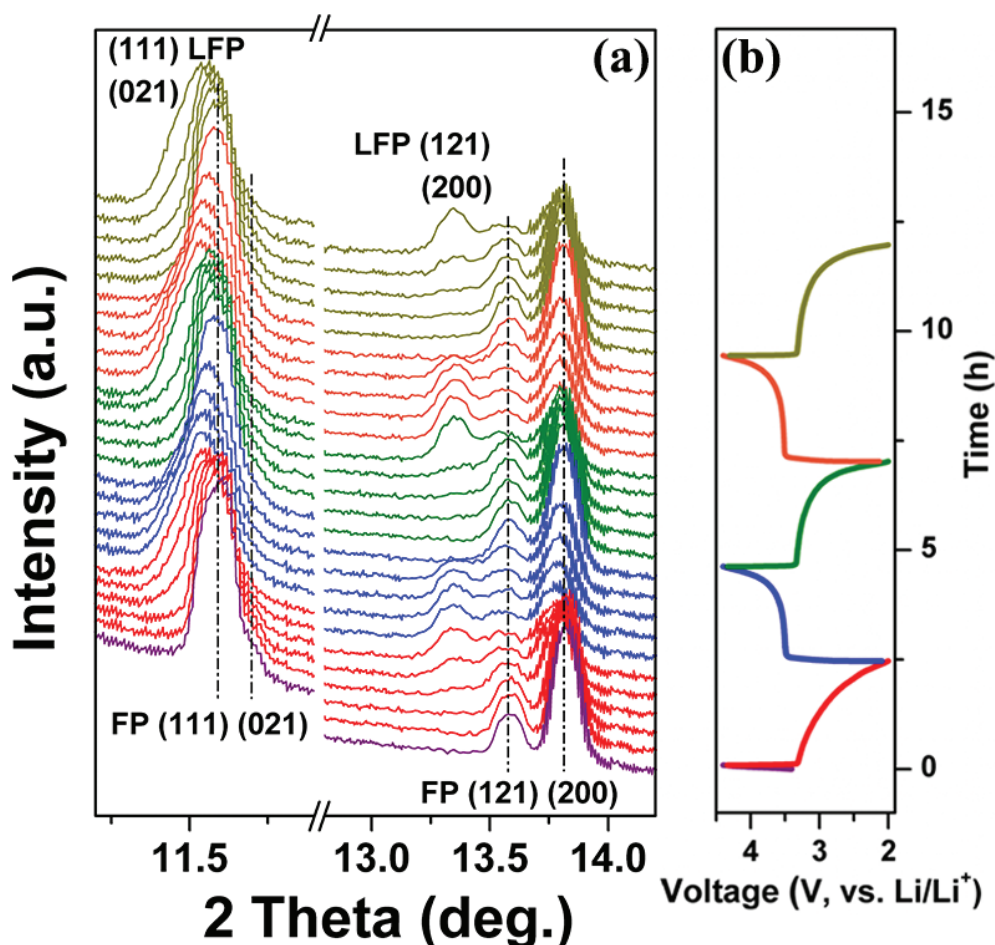
Figure 8. In-situ synchrotron XRD of A-FP along with galvanostatic cycling. (a) shows the enlarged (111), (021), (121), and (200) peaks; (b) shows the corresponding charge/discharge curves. The X-ray wavelength is 0.7018944 Å.

the specific surface area is clearly decreased. As a result, the battery performance is dramatically deteriorated because of the low Li^+ diffusion rate and the incomplete phase separation during charge/discharge. Note that a "self-healing" process with slight solid solution behavior is observed in the first several cycles possibly due to the re-equilibration of phase separation in terms of particle size, morphology, pore distribution, and even lattice strain. After chemical delithiation, nearly all the lithium is removed from A-LFP and the resulting $FePO_4$ preserves well the orthorhombic structure. The particle morphology does not change much compared with A-LFP, but the particles are more homogeneous, exhibiting a narrower size distribution. The ultralarge agglomerates in A-LFP are now crushed into small and uniform particles by the mechanical and chemical interactions during delithiation. Significant amounts of mesopores are generated and the specific surface area is noticeably increased. Therefore, the electrochemical performance recovers after several cycles of "self-healing". The battery performance is even comparable with that of pristine LFP although the particle morphology is not favorable for lithium diffusion anymore. However, the battery performance is dramatically degraded again by postannealing of FP at 300 °C for 24 h. The A-FP has a specific surface area of only half of that of FP although they have similar particle size and morphology. On the other hand, it has a sphere-like morphology that is not facile for lithium diffusion compared with the diamond-shaped pristine LFP although they have similar specific surface areas. What makes it worse is the pore size of A-FP moves to higher values with a

much wider distribution (20–300 nm) compared with both pristine LFP and FP. Thereby, the utilization of active material during lithium cycling is depressed. Consequently, A-FP shows an inferior performance with low capacity and sluggish Li^+ diffusion.

In conclusion, postannealing induces severe performance degradation of $Li_x FePO_4$ (x = 0, 1). The particle size, morphology, pore distribution, surface area, and probably lattice strain are noticeably changed after annealing. The electrochemical performance is therefore deteriorated due to the low Li^+ diffusion coefficient, difficult accessibility of electrolyte, and incomplete phase separation during charge/discharge. Moreover, a self-healing process with slight solid-solution behavior along with cycling is kept after annealing. These findings could also shed light on novel design of high density high performance cathode materials for rechargeable lithium batteries, e.g., platelet-stacked mesoporous $LiFePO_4$ micro-balls in combination with surface carbon coating and bulk doping may be of great promise.

3. Experimental

3.1. Material preparation

Pristine micro-sized $LiFePO_4$ was prepared by an optimized hydrothermal route;[33] 1.2 mol L^{-1} $LiOH \cdot H_2O$ (98+%, Alfa Aesar) was mixed with 0.4 mol L^{-1} H_3PO_4 (Aldrich) in deionized water. A little citric acid (99.5+%, Aldrich) was added to prevent the oxidation of Fe^{2+}. Next, 0.4 mol L^{-1} $FeSO_4 \cdot 7H_2O$ (99+%, Alfa Aesar) was slowly added under Ar protection. The pH value was adjusted to 7 by $LiOH \cdot H_2O$. The mixture was transferred into a Teflon-lined stainless steel autoclave and was held at 200 °C for 24 h. After natural cooling to room temperature, the product was washed and filtered several times with deionized water and ethanol alternatively. The final sample was collected by drying at 80 °C under vacuum for 12 h. It is denoted as LFP in this paper.

Pristine LFP was pressed into pellets with diameters of ∼10 mm. These pellets were sealed in an ampoule for overnight vacuuming. After high temperature annealing at 700 °C for 24 h, they were quenched by liquid nitrogen (N_2). The pellets were ground and collected with a designation of A-LFP.

Chemical delithiation of A-LFP was carried out by $NO_2 BF_4$ in acetonitrile;[36] 1.7 g of $NO_2 BF_4$ (100% excess) was dissolved in 100 mL of acetonitrile and 1 g of A-LFP was added. The mixture was vigorously stirred for 30 h at ambient temperature. The product was filtered and washed using methanol ($CH_3 OH$) several times, and was dried at 80 °C for 12 h under vacuum. The so-obtained sample is simply presented as FP.

The FP was then annealed at 300 °C for 24 h in air, and was cooled naturally to room temperature. The resulting material is marked as A-FP.

3.2. Structure characterization

High resolution synchrotron X-ray diffraction (XRD, λ = 0.7751922 Å) was employed to analyze the crystalline structure. The particle morphology was observed by an S-4800 (Hitachi) field emission scanning electron microscopy (FESEM). The particle size distribution was obtained by laser particle size analyzer at Xi'an Maxsun Kores New Materials Co., LTD. The Brunauer–Emmett–Teller (BET) surface area was characterized by an SA3100 surface area and pore size analyzer (Beckman Coulter). The nitrogen (N_2) adsorption-desorption isotherm was carried out by liquid N_2 at 77 K. In-situ synchrotron XRD during electrochemical charge/discharge was collected every 8 min with scans from 1.67° to 33.13° (2 theta, λ = 0.7018944 Å).

3.3. Electrochemical performance

Swagelok half cells using lithium metal as the anode were assembled in an Ar-filled glove box. The cathode consisted of Li_xFePO_4 (x = 0, 1), super P, and polytetrafluoroethylene (PTFE) in a weight ratio of 80:15:5. The electrolyte was 1 mol L^{-1} $LiPF_6$ in ethylene carbonate/dimethyl carbonate (EC/DMC, 1:1), and the separator was Celgard 2500. The batteries were cycled with constant currents on an Arbin BT2000 at room temperature. The electrochemical impedance spectroscopy (EIS) was collected by a Versatile Multichannel Galvanostat 2/Z (VMP2, Princeton Applied Research) in the frequency range from 10^{-2} Hz to 10^5 Hz.

Acknowledgments

References

1. Armand, M.; Tarascon, J. M. *Nature* **2008**, *451*, 652–657.

2. Whittingham, M. S. *Proc. IEEE* **2012**, *100*, 1518–1534.

3. Dunn, B.; Kamath, H.; Tarascon J. M. *Science* **2011**, *334*, 928–935.

4. Goodenough, J. B. *J. Solid State Electrochem.* **2012**, *16*, 2019–2029.

5. Cheng, F. Y.; Liang, J.; Tao, Z. L.; Chen J. *Adv. Mater.* **2011**, *23*, 1695–1715.

6. Kang K. S.; Meng, Y. S.; Breger, J.; Grey, C. P.; Ceder, G. *Science* **2006**, *311*, 977–980.

7. Kraytsberg, A.; Ein-Eli, Y. *Adv. Energy Mater.* **2012**, *2*, 922–939.

8. Gong, Z. L.; Yang, Y. *Energy Environ. Sci.* **2011**, *4*, 3223–3242.

9. Nyten, A.; Abouimrane, A.; Armand, M.; Gustafsson, T.; Thomas, J. O. *Electrochem. Commun.* **2005**, *7*, 156–160.

10. Kim, J. C.; Moore, C. J.; Kang, B.; Hautier, G.; Jain, A.; Ceder, G. *J. Electrochem. Soc.* **2011**, *158*, A309–A315.

11. Sun, X.; Xu, Y.; Jia, M.; Ding, P.; Liu, Y.; Chen, K. *J. Mater. Chem. A* **2013**, *1*, 2501–2507.

12. Barpanda, P.; Ati, M.; Melot, B. C.; Rousse, G.; Chotard, J. N.; Doublet, M. L.; Sougrati, M. T.; Corr, S. A.; Jumas, J. C.; Tarascon, J. M. *Nat. Mater.* **2011**, *10*, 772–779.

13. Goodenough, J. B.; Kim, Y. *Chem. Mater.* **2010**, *22*, 587–603.

14. Manthiram, A. *J. Phys. Chem. Lett.* **2011**, *2*, 176–184.

15. Padhi, A. K.; Nanjundaswamy, K. S.; Goodenough, J. B. *J. Electrochem. Soc.* **1997**, *144*, 1188–1194.

16. Park, O. K.; Cho, Y.; Lee, S.; Yoo, H. C.; Song, H. K.; Cho, J. *Energy Environ. Sci.* **2011**, *4*, 1621–1633.

17. Morgan, D.; Ven, A. V. d.; Ceder, G. *Electrochem. Solid-State Lett.* **2004**, *7*, A30–A32.

18. Islam, M. S.; Driscoll, D. J.; Fisher, C. A. J.; Slater, P. R. *Chem. Mater.* **2005**, *17*, 5085–5092.

19. Nishimura, S. I.; Kobayashi, G.; Ohoyama, K.; Kanno, R.; Yashima, M.; Yamada, A. *Nat. Mater.* **2008**, *7*, 707–711.

20. Andersson, A. S.; Thomas, J. O. *J. Power Sources* **2001**, *97–98*, 498–502.

21. Guoying, C.; Xiangyun, S.; Thomas, J. R. *Electrochem. Solid-State Lett.* **2006**, *9*, A295–A298.

22. Laffont, L.; Delacourt, C.; Gibot, P.; Wu, M. Y.; Kooyman, P.; Masquelier, C.; Tarascon, J. M. *Chem. Mater.* **2006**, *18*, 5520–5529.

23. Delmas, C.; Maccario, M.; Croguennec, L.; Le Cras, F.; Weill, F. *Nat. Mater.* **2008**, *7*, 665–671.

24. Yamada, A.; Koizumi, H.; Nishimura, S. I.; Sonoyama, N.; Kanno, R.; Yonemura, M.; Nakamura, T.; Kobayashi, Y. *Nat. Mater.* **2006**, *5*, 357–360.

25. Gu, L.; Zhu, C.; Li, H.; Yu, Y.; Li, C.; Tsukimoto, S.; Maier, J.; Ikuhara, Y. *J. Am. Chem. Soc.* **2011**, *133*, 4661–4663.

26. Malik, R.; Zhou, F.; Ceder, G. *Nat. Mater.* **2011**, *10*, 587–590.

27. Bai, P.; Cogswell, D. A.; Bazant, M. Z. *Nano Lett.* **2011**, *11*, 4890–4896.

28. Wang, J.; Sun, X. *Energy Environ. Sci.* **2012**, *5*, 5163–5185.

29. Kang, B.; Ceder, G. *Nature* **2009**, *458*, 190–193.

30. Chung, S. Y.; Bloking, J. T.; Chiang, Y. M. *Nat. Mater.* **2002**, *1*, 123–128.

31. Gibot, P.; Casas-Cabanas, M.; Laffont, L.; Levasseur, S.; Carlach, P.; Hamelet, S.; Tarascon, J. M.; Masquelier, C. *Nat. Mater.* **2008**, *7*, 741–747.

32. Malik, R.; Burch, D.; Bazant, M.; Ceder, G. *Nano Lett.* **2010**, *10*, 4123–4127.

33. Sun, X.; Xu, Y.; Liu, Y.; Li, L. *Acta Phys.-Chim. Sin.* **2012**, *28*, 2885–2892.

34. Sun, X. F.; Xu, Y. L. *Mater. Lett.* **2012**, *84*, 139–142.

35. Yang, S.; Song, Y.; Zavalij, P. Y.; Whittingham, M. S. *Electrochem. Commun.* **2002**, *4*, 239–244.

36. Sun, X.; Xu, Y.; Chen, G.; Li, T.; Jia, M.; Li, L. *Chinese. J. Inorg. Chem.* **2013**, online, DOI: 10.11862/CJIC.2014.160.

37. Zhu, C.; Yu, Y.; Gu, L.; Weichert, K.; Maier, J. *Angew. Chem. Int. Edn* **2011**, *50*, 6278–6282.

38. Wang, X. J.; Jaye, C.; Nam, K. W.; Zhang, B.; Chen, H. Y.; Bai, J.; Li, H.; Huang, X.; Fischer, D. A.; Yang, X. Q. *J. Mater. Chem.* **2011**, *21*, 11406–11411.

39. Cogswell, D. A.; Bazant, M. Z. *ACS Nano* **2012**, *6*, 2215–2225.

40. Burch, D.; Bazant, M. Z. *Nano Lett.* **2009**, *9*, 3795–3800.